Mechanical response of an adaptive solar timber stadium structure

Rana Nazifi Charandabi[a,*], Gerardo Carpentieri[b], Fernando Fraternali[b]

[a]*Department of Information Engineering, Electrical Engineering and Applied Mathematics, University of Salerno, 84084 Fisciano(SA), Italy*
[b]*Department of Civil Engineering, University of Salerno, 84084 Fisciano (SA), Italy*

Abstract

This work proposes a novel structural concept for sports stadiums based on a remarkably long-span timber system combined with an adaptive, sun-tracking roof. Cable pretension in the glued laminated timber supporting structure is introduced as a key design parameter to regulate structural stiffness and enhance overall mechanical performance. The roof assembly incorporates a tiltable solar membrane equipped with lightweight, bifacial photovoltaic devices. A design methodology is presented for the key modular elements of the supporting timber structure, including minimum-mass-oriented sizing of the structural members and a detailed definition of the prestressing strategy associated with a representative mast element. The structural response under wind loading is investigated using a nonlinear continuation technique capable of tracking equilibrium paths in the presence of follower forces and predicting the vibration modes of the system. The results indicate stable behavior under high wind loads and sufficiently separated modal frequencies, with a fundamental frequency on the order of 2 Hz. The tensegrity-based modeling framework is validated through a three-dimensional finite element simulation of a representative stadium module, which captures the spatial response and transverse vibration modes of the

*Corresponding author. Email: rnazificharandabi@unisa.it

URL: rnazificharandabi@unisa.it (Rana Nazifi Charandabi), gerardo_carpentieri@msn.com (Gerardo Carpentieri), f.fraternali@unisa.it (Fernando Fraternali)

This manuscript is a preprint of the following published article: R. Nazifi Charandabi, G. Carpentieri, and F. Fraternali, 'Mechanical response of an adaptive solar timber stadium structure', Mechanics of Advanced Materials and Structures, vol. 33, no. 1, article 2644538, 2026. The Version of Record is available at https://doi.org/10.1080/15376494.2026.2644538

structure. Overall, the proposed timber–tensegrity solution demonstrates favorable stiffness, stability, and dynamic performance for sustainable, solar-integrated stadium structures.

Keywords: Tensegrity, Solar stadiums, Prestress, Solar membrane, Wind forces

1. Introduction

Sports stadiums form a demanding class of large-span structures, characterized by stringent serviceability requirements and pronounced sensitivity to self-weight and environmental actions (see, e.g., Tahmasebinia et al., 2023 and references therein). From a life-cycle perspective, they are also among the most carbon-intensive building typologies (Xuan et al., 2025). Even a single match event has been shown to generate significant environmental impacts (Daddi et al., 2025). Recent assessments indicate that embodied carbon associated with primary structural systems represents a dominant contribution to the overall environmental footprint of stadiums, often comparable to or exceeding operational emissions (Xuan et al., 2025; FIFA, 2023). These findings motivate the exploration of alternative structural solutions capable of reducing material-related emissions while maintaining mechanical efficiency (Dong et al., 2020b; Alaoui and Zarraa, 2025; Sustainability Magazine, 2023).

Engineered timber systems have emerged as efficient and sustainable solutions for stadium supporting structures (Dong et al., 2020b; Dodoo et al., 2014; FIFA, 2023). Life-cycle analyses indicate that glued laminated timber (GLT) and related products can achieve substantial reductions in embodied carbon compared to conventional steel–concrete systems, owing to lower production energy requirements and inherent carbon storage capacity (Dong et al., 2020b). The favorable strength-to-weight ratio of timber is particularly advantageous for long-span structural applications. The feasibility of timber-based stadium structures has been demonstrated by several realized case studies, among which Westhills Stadium, located in Langford, Canada, stands out as a particularly significant example and serves as a source of inspiration for the present study (FIFA, 2023; Sport & Impianti, 2023). Of particular interest are the stadium designs developed by BEAR Stadiums in collaboration with Rubner Holzbau, which are presented on the company's website (BEAR Stadiums).

Roof systems further influence both structural behavior and operational

sustainability. Lightweight tensile membrane roofs efficiently cover large spans through prestress and geometry, while their mechanical response has been shown to depend strongly on form-finding and prestress optimization (Bridgens and Birchall, 2012; Milošević et al., 2024). When combined with photovoltaic technologies, and particularly with adaptive sun-tracking strategies, membrane roofs can significantly enhance on-site energy generation, while introducing additional challenges related to geometric nonlinearity and coupled structural–energy interactions (Scotta et al., 2016; Marchwiński et al., 2023; Charandabi et al., 2025a,b).

The present study addresses the design and mechanical modeling of the key modular components of an innovative glued laminated timber (GLT) stadium supporting structure. The analyzed timber system is integrated with a solar membrane that can be optimally tilted by means of two suspension cables made of steel wire ropes (Sirtef srl, 2026). The structure adopts a tensegrity-based architectural concept and can be internally prestressed through controlled prestretching of the steel cables, which enhances the overall stiffness of the system. With the sole exception of the steel wire ropes, the structural masts are entirely composed of GLT members. The main novelty of the present study, with respect to recent works on sun-tracking solar stadium roofs (Charandabi et al., 2025a,b), lies in the adoption of a highly sustainable timber supporting structure with a considerably long span in place of a conventional steel system, together with the use of a solar membrane equipped with thin, semiflexible photovoltaic (PV) panels on both faces (Solbian, 2025). As a result, the proposed sun-tracking roof system enables the capture of both diffuse and ground-reflected components of solar radiation. The paper focuses on the response of the main elements of the GLT stadium structure to normal wind forces, while the analysis of drag-type wind forces and the mechanical response of the solar membrane are deferred to future work. Section 2 presents the conceptual design of a mast element of the stadium structure under investigation, together with a minimum-mass sizing procedure for the cross sections of the structural members. The prestressing scheme of the system is described in Sect. 3. A path-following procedure capable of handling the tensegrity-type mechanical modeling of the mast structure subjected to follower-type wind forces is then introduced in Sect. 4. The path-following procedure is employed in Sect. 5 to investigate the mechanical response of the mast element under wind loading up to failure (Sect. 5.1), and to analyze the vibration modes of the structural system (Sect. 5.2). The tensegrity-based modeling is complemented

by a three-dimensional finite element analysis of the vibration modes of a spatial modular element of the solar stadium structure, presented in Sect. 6. This analysis employs beam elements to model the structural members and enables the investigation of transverse vibration modes of the structure (Ashwear et al., 2016). The paper concludes with a discussion of the results and an outline of future research directions in Sect. 7.

2. Conceptual design and member sizing

The stadium structure studied in the present work is designed around a series of structural masts, spaced longitudinally at 6 m intervals and having a total height of 35 m in the reference configuration, from which the main GLT member protrudes orthogonally over a span of 20 m. The masts are composed of GLT members mutually connected through hinged joints and are integrated with two steel wire ropes of type VEROTOP P manufactured by Sirtef srl. These ropes have a nominal diameter of 76 mm, a minimum breaking load of 5451 kN, an elastic modulus of 93 GPa, a metallic area of 3311.62 mm^2, and a linear mass density of 28.30 kg/m, as specified by the manufacturer (Sirtef srl, 2026). The ropes act as suspension cables for the main GLT bar (hereafter also referred to as the main beam). Let α denote the angle formed by this beam with the horizontal plane, measured positively counterclockwise. Figure 1(a) shows the node numbering of a mast element for $\alpha = 0$, while Fig. 1(b) illustrates three different configurations corresponding to $\alpha = 0$, $\alpha = -30°$, and $\alpha = 45°$. These configurations are achieved by connecting the two steel cables 6–17 and 8–17 to one or two winches that suitably adjust their free lengths, thus attaining the desired inclination angle α. The same winch systems can also be used on site to prestress the cables and to lock the deployment mechanism once the optimal membrane orientation has been achieved. During the actuation process that modifies the tilting angle α, the main GLT beam 7–17 undergoes rigid-body motion.

The tensegrity systems forming the mast structures shown in Fig. 1 are assumed to comprise two parallel and identical planar trusses, sufficiently spaced in the longitudinal x direction, which is parallel to the playing field. Together, these trusses form a sandwich-type structural system that incorporates the main beam 7–17. Each truss is composed of seven panels, with a size of 4 m in the y direction and 5 m in the z direction of the transverse plane. The main beam is connected to a solar membrane covering an area

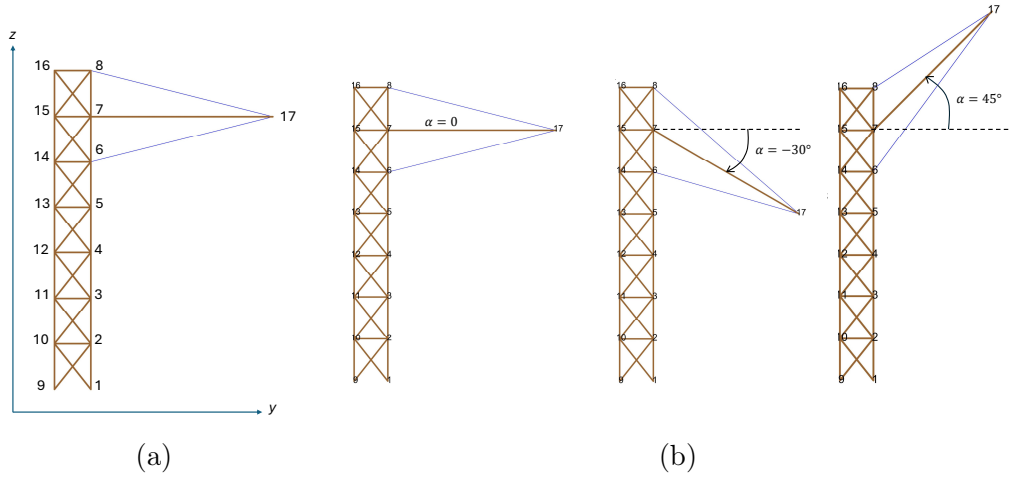

(a) (b)

Figure 1: (a) Node numbering of the generic stadium support mast structure. (b) Reference configurations of the mast structure for different values of the roof membrane inclination angle α, including flat, downward-sloping, and upward-sloping configurations.

of 6 m × 20 m, consisting of a Serge Ferrari Group Flexlight Xtrem TX30-II membrane with an areal mass density of 1.05 kg/m^2 (Serge Ferrari Group, 2024). Although a detailed mechanical analysis of the membrane is not addressed in the present contribution and is deferred to future work, a preliminary design of this component, carried out in collaboration with IXRAY Ltd. (2024), predicts the adoption of a uniform biaxial prestress of 1 daN/m in both the warp and weft directions. The photovoltaic cells applied to the membrane surfaces are assumed to consist of 1054 mm × 800 mm × 2 mm SunBender SB 47 panels manufactured by Solbian, each with a mass of 2 kg (Solbian, 2025). The resulting overall areal weight of the membrane–PV assembly is assumed to be equal to 60 N/m^2. These panels exhibit considerable flexibility and are capable of accommodating a central deflection of up to 122 mm over an arc length of 1 m (Solbian Manual, 2025).

Previous studies have shown that varying the slope of photovoltaic (PV) panels installed on the roofs of solar stadiums throughout the day and across different months of the year leads to substantial increases in solar energy harvesting capacity compared with fixed-slope configurations. Such increases may range between 50% and 80% when comparing peak power output with wintertime power generation (Charandabi et al., 2025a,b). Similar performance improvements are reasonably expected for the sun-tracking solar mem-

brane roof investigated in the present study. In addition, further energy gains may be anticipated due to the adoption of bifacial PV panels, an aspect not addressed in the aforementioned literature. A detailed assessment of the solar energy harvesting capacity of the proposed stadium structure is, however, addressed to future work, as this topic lies beyond the scope of the present paper.

The GLT members are made of glued laminated timber of strength class GL28h, in accordance with Eurocode 5 (EC5, European Committee for Standardization - EC5 (2004)), with a mass density of $\rho = 425$ kg/m^3. The characteristic compressive and tensile strengths parallel to the grain are $f_{c,0,k} = 28$ MPa and $f_{t,0,k} = 22.3$ MPa, respectively, while the characteristic bending strength is $f_{m,k} = 28$ MPa, in agreement with the provisions of EC5 and the Italian technical standard for timber structures NTC (2018) (see, e.g., Binderholz GmbH (2024)). The global tensegrity and finite element analyses presented in Sects. 5–6 employ the following elastic moduli, consistent with EC5: elastic modulus parallel to the grain $E_{0,\text{mean}} = 12.6$ GPa; elastic modulus perpendicular to the grain $E_{90,\text{mean}} = 0.30$ GPa; and shear modulus $G_{\text{mean}} = 0.65$ GPa. The direction of the grain is assumed to be parallel to the axes of the GLT members.

Once the conceptual design phase was completed, a minimum-mass algorithm was employed to size the GLT members, following the procedure outlined in Nagase and Skelton (2014), suitably adapted to the present case (see also Charandabi et al. (2025a), where it was applied to a different stadium design). The approach consists of minimizing the overall mass m of the system as a linear function of the force densities x_i (axial force per unit length) of all n_x members, i.e.,

$$m = \mathbf{c}^T \mathbf{x}, \tag{1}$$

where $\mathbf{x}$ is the vector collecting the force densities of all members, and $\mathbf{c}$ is a vector whose generic entry c_i is defined as

$$c_i = \frac{\rho_i, \ell_i^2}{\sigma_i}, \tag{2}$$

Here, ℓ_i denotes the length of the i-th member, ρ_i is the corresponding mass density, and σ_i is the design stress. The minimum-mass procedure employs a linear programming algorithm to minimize the objective function (1) under equilibrium constraints, which enforce satisfaction of the nodal equilibrium equations for one or multiple loading conditions. In the present case,

the structural members are identified as the GLT components of the structural mast (hereafter referred to as bars) and the suspension steel wire ropes (hereafter referred to as strings). The latter are assigned a predefined size characterized by a nominal diameter of 76 mm, as previously anticipated (Sirtef srl, 2026). The adopted procedure defines the design stress of the compressed GLT members as the ultimate limit state (ULS) design stress $k_{\text{crit}} f_{c,0,d}$, where $f_{c,0,d} = k_{mod} k_h f_{c,0,k}/\gamma_M$, with $\gamma_M = 1.45$ denoting the ULS partial material safety factor, and k_{crit} being the reduction factor accounting for buckling failure in accordance with Section 4.4.8.2.2 of NTC (2018). For GLT members subjected to tension, the design stress is identified with $f_{t,0,d} = k_{mod} k_h f_{t,0,k}/\gamma_M$. In the present study, $k_{mod} = 0.90$ and $k_h = 1.00$ are adopted, in accordance with NTC (2018). Finally, the suspension cables are designed for a ULS design tensile force of $N_{t,\text{Rd}} = 5451/5.0 = 1090$ kN, corresponding to the minimum breaking load divided by a safety factor of 5.0 (European Committee for Standardization (CEN) - EN 12385).

The minimum-mass algorithm iteratively minimizes the objective function (1) by updating the ULS design compressive stress as a function of the current design iteration of the compressed members, following the approach described in Nagase and Skelton (2014). For each of the three configurations shown in Fig. 1, such a procedure was carried out under permanent (gravity) loads multiplied by a ULS safety factor γ_G and wind forces applied at nodes 7 and 17, multiplied by a ULS safety factor γ_Q. The permanent loads consist of nodal forces that lump, at the end nodes of each member, its self-weight and include the self-weight of the solar membrane associated with bar 7–17. The wind loads consist of two forces directed perpendicular to the member 7–17 and acting either downward (*'downward wind' loading condition*) or upward (*'upward wind' loading condition*). Their magnitude is determined by applying a reference wind pressure $q_{\text{wind}} = 1.0$ kN/m^2 to the solar membrane, a value commonly adopted in studies of the mechanical response of tensile membranes under wind loading (Bridgens and Birchall, 2012; Milošević et al., 2024). We assumed $\gamma_G = 1.3$ and $\gamma_Q = 1.5$ in the case of downward wind forces, as well as $\gamma_G = 1.0$ and $\gamma_Q = 1.5$ for upward wind forces, in accordance with (NTC, 2018).

The adopted design procedure resulted in the following member sizes, selected as the maximum values among those obtained for the three configurations shown in Fig. 1, after homogenizing the results across the different typologies of GLT members. The main GLT beam 15–7–17 was assigned a cross section of 800 mm $\times$ 300 mm; the columns of each of the two sandwich

trusses forming the mast were assigned a cross section of 300 mm × 800 mm; and the horizontal and diagonal members of these trusses were assigned a cross section of 260 mm × 800 mm. By convention, the first dimension of each cross section refers to the dimension lying in the transverse y–z plane shown in Fig. 1.

The Computer-Aided Design (CAD) drawings shown in Figs. 2–3, developed using *Rhinoceros 3D*®, illustrate a three-dimensional modular stadium unit designed through the minimum-mass sizing procedure (Fig. 2) and the overall stadium configuration composed of four independent grandstands arranged in a rectangular plan (Fig. 3). Figure 2(a)–(c) show the tilting of the roof obtained by varying the inclination angle α, while the side view, front view, and an axonometric view for $\alpha = 0°$ are reported in Figs. 2(d)–(f), respectively.

The three-dimensional stadium structure includes longitudinal GLT links connecting adjacent mast sections in both the horizontal and vertical planes, thereby ensuring the overall stability of the structure. The connections between GLT elements, including lacing members, are realized using slotted-in steel plates and dowels (see, e.g., Dong et al. (2020a)).

3. Prestressing scheme of a mast element

Let us consider the mechanical response of a mast element in the y–z plane by modeling the sandwich trusses as a single equivalent element with doubled cross-sectional areas for the columns, horizontal members, and diagonal members forming each individual truss. It can be readily shown that, when the deployment mechanism is locked, the structure does not exhibit kinematic mechanisms and has a degree of static indeterminacy equal to seven, implying that it admits seven independent self-stress modes. Only one of these modes is governed by the prestretching of the suspension cables 6–17 and 7–17 and is assumed to represent the tensegrity prestress mode of the structural mast. Figure 4 graphically illustrates the prestress modes corresponding to the configurations with $\alpha = 0$, $\alpha = -30°$, and $\alpha = 45°$.

The use of a *Mathematica*® code to solve the equilibrium equations of the structure in the absence of external loads led to the derivation of the expressions reported in Eqns. (3)–(5) for the only nonzero force-densities associated with the solutions illustrated in Fig. 4. In these expressions, x_1 denotes the independent variable, and the adopted sign convention assumes force densities to be positive in tension for the suspension cables and positive

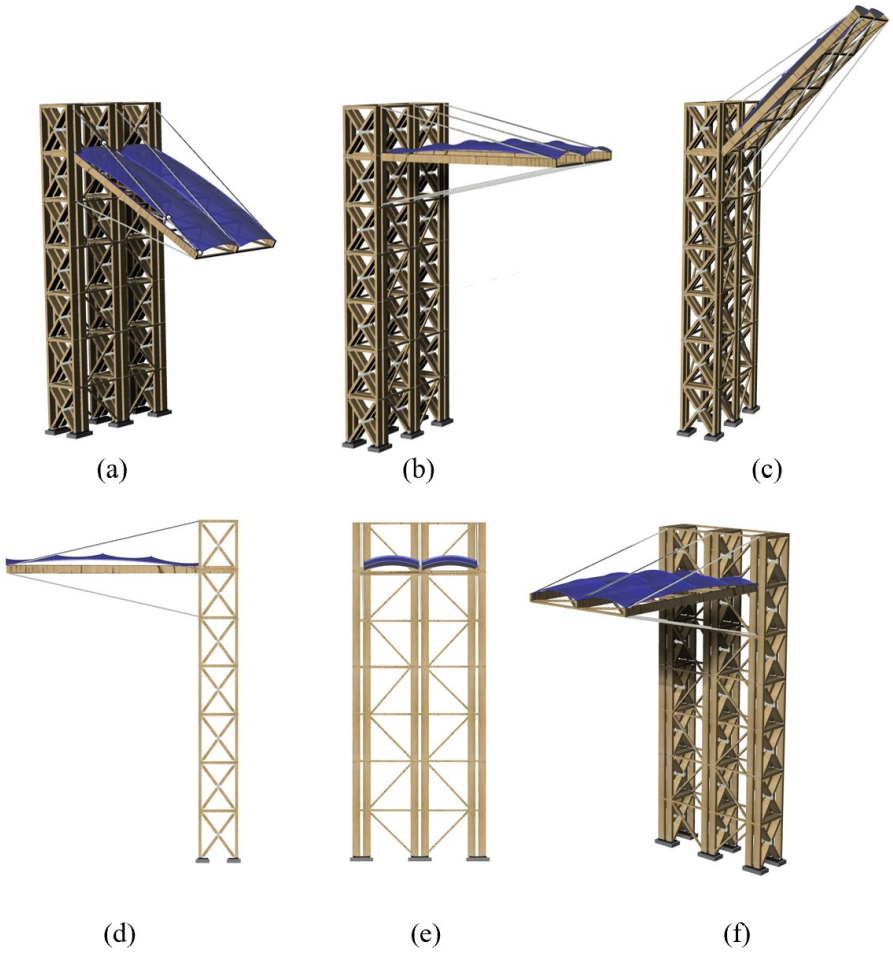

Figure 2: Different views of a modular component of the GLT stadium structure, composed of three adjacent mast structures. (a–c) Views illustrating the tilting of the roof obtained by varying the inclination angle from $\alpha = -30°$ (a) to $\alpha = 0°$ (b) and $\alpha = 45°$ (c). (d) Side view. (e) Front view. (f) Axonometric view for $\alpha = 0°$.

in compression for the GLT members. The latter may carry either compressive or tensile forces, whereas the suspension cables are assumed to carry tensile forces only.

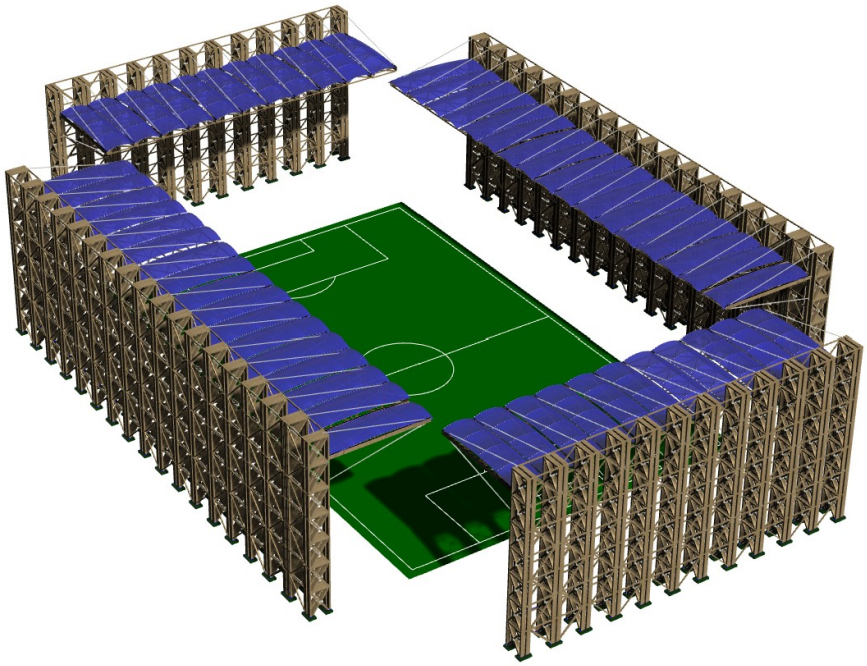

Figure 3: Global view of a stadium structure composed of four timber grandstands arranged in a rectangular plan, with $\alpha = 0$ assumed for each grandstand. The long grandstands consist of 18 mast units, while the short grandstands consist of 12 mast units. The longitudinal spacing between adjacent masts is 6 m, and the overall height of the structure is 35 m. The seating tiers are omitted for clarity of the structural representation.

$$\begin{aligned} \alpha = 0. \quad & 6-17, 8-17, 6-15: \ x_1; \quad 7-17, 7-8: \ 2x_1; \\ & 14-15, 6-14: \ -6x_1; \quad 15-16, 8-16: \ -4x_1; \\ & 7-16: \ 4x_1; \quad 7-14: \ 6x_1; \quad 8-15: \ -x_1 \end{aligned} \tag{3}$$

$$\begin{aligned} \alpha = -30^\circ. \quad & 6-17, 8-17, 6-15: \ x_1; \quad 7-17, 7-8: \ 2x_1; \\ & 14-15, 6-14: \ -3.33x_1; \quad 15-16, 8-16: \ -5.33x_1; \\ & 7-16: \ 5.33x_1; \quad 7-14: \ 3.33x_1; \quad 8-15: \ x_1 \end{aligned} \tag{4}$$

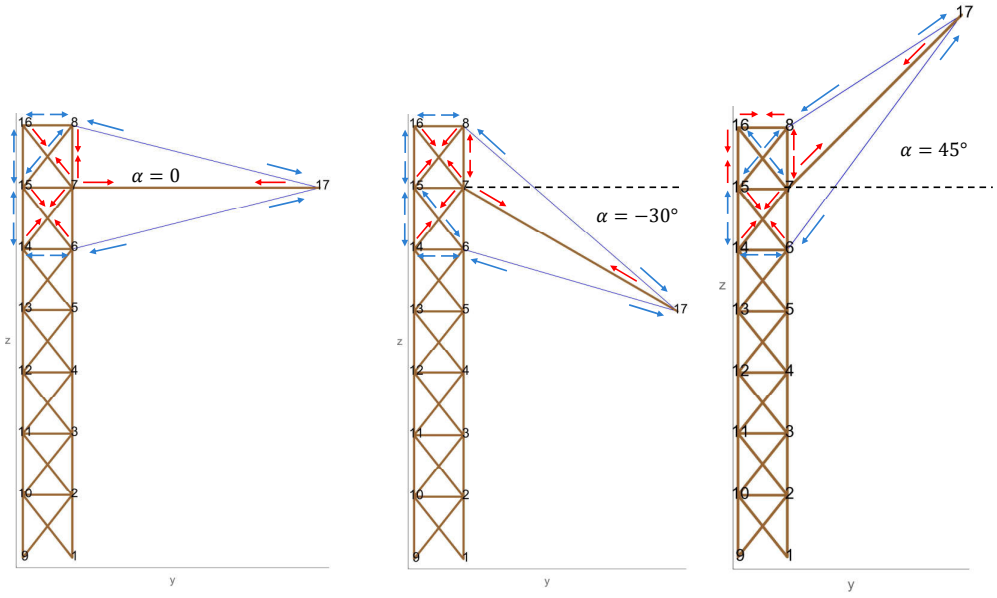

Figure 4: Prestress schemes corresponding to different values of the roof inclination angle, α, as induced by the pretensioning of cables 6–17 and 8–17. The forces shown represent member axial forces: red arrows denote compression, while blue arrows indicate tension.

$$\begin{aligned}\alpha = 45°.\quad & 6-17, 8-17:\ x_1;\quad 7-17, 7-8:\ 2x_1;;\quad 6-15:\ 3.83x_1;\\ & 14-15, 6-14:\ -7.36x_1;\quad 15-16, 8-16:\ 0.29x_1;\\ & 7-16:\ -0.29x_1;\quad 7-14:\ 7.36x_1;\quad 8-15:\ -3.83x_1 \end{aligned} \tag{5}$$

4. Path-following procedure accounting for follower forces

This section formulates a path-following procedure to analyze the quasi-static deformation process of a tensegrity-based model of the mast structure under normal wind forces. The proposed procedure generalizes that presented in Fraternali et al. (2015a) to account for the presence of follower-type forces. We analyze the equilibrium equations of the mast structure by assuming that it consists of a total of M bars and strings and exhibits two degrees of freedom per node, with the analysis restricted to the response in the transverse y–z plane. By modeling bars and strings as elastic members acting under axial forces, the equilibrium equation associated with a generic

degree of freedom p can be written as follows

$$r_p \;=\; \sum_{m=1}^{M} k_m \left(\ell_m - \bar{\ell}_m\right) \frac{\partial \ell_m}{\partial u_p} \;-\; \lambda\; q_p(\boldsymbol{u}) \;-\; g_p = 0, \tag{6}$$

In Eqn. (6), r_p denotes the p-th component of the *residual vector* $\boldsymbol{r}$, while ℓ_m denotes the length of member m in the current (deformed) configuration and $\bar{\ell}_m$ denotes its rest length in the stress-free configuration. The parameter k_m is the elastic axial stiffness coefficient of member m, defined as the elastic modulus of the member in the axial direction multiplied by its cross-sectional area and divided by its rest length; it is assumed to remain constant during the deformation process. The quantity u_p denotes the p-th component of the nodal displacement vector $\boldsymbol{u}$. The vector $\boldsymbol{q}$, with generic entry q_p, collects a reference set of wind-induced nodal forces, which are assumed to act in the direction normal to the current configuration of the members (follower forces) and to be proportional to the load multiplier λ. The vector $\boldsymbol{g}$, with generic entry g_p, instead collects the nodal forces associated with permanent dead loads. We assume that string elements (i.e., the suspension cables of the mast structure) can carry tensile forces only. This assumption is enforced by setting the stiffness coefficient k_m equal to zero whenever the current length ℓ_m of a string is smaller than its rest length $\bar{\ell}_m$. The m-th member connects nodes i and j and is oriented from node i to node j. We can therefore write

$$\begin{aligned} \ell_m = \Big\{ &\left[(x_j + u_j) - (x_i + u_i)\right]^2 + \left[(y_j + v_j) - (y_i + v_i)\right]^2 \\ &+ \left[(z_j + w_j) - (z_i + w_i)\right]^2 \Big\}^{1/2} \end{aligned} \tag{7}$$

Here, x_i, y_i, z_i and x_j, y_j, z_j denote the Cartesian coordinates of nodes i and j, respectively, in a given reference configuration with respect to the adopted Cartesian reference frame (x, y, z). The quantities u_i, v_i, w_i and u_j, v_j, w_j instead denote the Cartesian components of the displacement vectors of the same nodes measured from the reference configuration.

The wind load vector $\boldsymbol{q}(\boldsymbol{u})$ is obtained by assembling the contributions arising from the individual members forming the structure. Accounting for the follower-type nature of the wind forces, the contribution associated with the m-th member is described by the following entries, which are dual to the displacement components of nodes i and j

$$\text{entries dual of } v_i, v_j: \quad \gamma_Q \frac{q_{\text{wind}} a_m}{2} \left[(z_j + w_j) - (z_i + w_i)\right], \tag{8}$$

$$\text{entries dual of } w_i, w_j: \; -\gamma_Q \frac{q_{wind} a_m}{2} \left[(y_j + v_j) - (y_i + v_i) \right] \tag{9}$$

a_m denoting the length in the x-direction of the portion of the solar membrane acting on member m.

We now formulate a continuation procedure to iteratively solve the equilibrium equations (6) associated with all the degrees of freedom of the structure. This procedure consists of solving the following *extended system* of equilibrium equations (Fraternali et al., 2015a)

$$\hat{\boldsymbol{r}} = \left[\boldsymbol{r}(\boldsymbol{u}, \lambda) \; f(\boldsymbol{u}, \lambda) \right]^T = \boldsymbol{0} \tag{10}$$

where the superscript T denotes transposition, and $f(\boldsymbol{u}, \lambda) = 0$ represents a suitable constraint equation describing the deformation process under consideration. In the case of a load-control process, which is considered in the next section, one assumes

$$f(\boldsymbol{u}, \lambda) := \lambda - c = 0, \tag{11}$$

where c is a prescribed constant. An iterative Newton–Raphson correction scheme is employed to solve Eqn. (10), starting from an initial point $\boldsymbol{u} = \bar{\boldsymbol{u}}$ and $\lambda = \bar{\lambda}$. The scheme is based on the following linearization

$$\hat{\boldsymbol{r}} = \hat{\bar{\boldsymbol{r}}} + \begin{bmatrix} \nabla_u \boldsymbol{r} & \nabla_\lambda \boldsymbol{r} \\ \nabla_u f & \nabla_\lambda f \end{bmatrix} \begin{bmatrix} \Delta u \\ \Delta \lambda \end{bmatrix} = \boldsymbol{0} \tag{12}$$

where $\hat{\bar{\boldsymbol{r}}} = [\bar{\boldsymbol{r}} \;\; \bar{f}]^T$, with $\bar{\boldsymbol{r}} = \boldsymbol{r}\left(\bar{\boldsymbol{u}}, \bar{\lambda}\right)$, and $\bar{f} = f\left(\bar{\boldsymbol{u}}, \bar{\lambda}\right)$. The quantity $\boldsymbol{K}_T = \nabla_u \boldsymbol{r}$ is the *tangent stiffness matrix* of the system. Let t_m denote the axial force in the generic member m, which is given by

$$t_m = k_m \left(\ell_m - \bar{\ell}_m \right), \tag{13}$$

and results from the given prestress state in correspondence to the reference configuration. The generic entry $k_{T_{ps}}$ of the tangent stiffness matrix is computed as follows:

$$k_{T_{ps}} = k_{M_{ps}} + k_{G_{ps}} + k_{L_{ps}}, \tag{14}$$

where

$$k_{M_{ps}} = \sum_m k_m \frac{\partial \ell_m}{\partial u_p} \frac{\partial \ell_m}{\partial u_s}, \tag{15}$$

$$k_{G_{ps}} = \sum_m t_m \frac{\partial^2 \ell_m}{\partial u_p \, \partial u_s}, \tag{16}$$

$$k_{L_{ps}} = -\frac{\partial q_p}{\partial u_s} \tag{17}$$

denote the entries of the components of the tangent stiffness matrix commonly referred to as the material stiffness matrix, the geometric stiffness matrix, and the load stiffness matrix, respectively (see, e.g., Fraternali et al. (2015b) and references therein). It is worth noting that, in the presence of follower forces, the load stiffness matrix is generally nonsymmetric (Timoshenko and Gere, 2012; Belytschko et al., 2014). The quantities defined by Eqns. (15)–(17) can be readily computed through a *Mathematica*® script, making use of Eqns. (7)-(9).

Upon observing that $\nabla_\lambda \boldsymbol{r} = -\boldsymbol{q}$ and setting $\bar{\boldsymbol{q}} = \boldsymbol{q}\,(\bar{\boldsymbol{u}})$, we rewrite Eqn. (12) as follows

$$\boldsymbol{K}_T \Delta \boldsymbol{u} - \Delta\lambda \bar{\boldsymbol{q}} = -\bar{\boldsymbol{r}}, \tag{18}$$

$$\nabla_u f \cdot \Delta \boldsymbol{u} + \nabla_\lambda f \, \Delta\lambda = -\bar{f} \tag{19}$$

We now denote by $\Delta \boldsymbol{u}_r$ and $\Delta \boldsymbol{u}_q$ the solutions of the linear systems

$$\boldsymbol{K}_T \Delta \boldsymbol{u}_r = -\bar{\boldsymbol{r}}, \tag{20}$$

$$\boldsymbol{K}_T \Delta \boldsymbol{u}_q = \bar{\boldsymbol{q}} \tag{21}$$

Once these solutions have been computed, one can write

$$\Delta \boldsymbol{u} = \Delta \boldsymbol{u}_r + \Delta\lambda \, \Delta \boldsymbol{u}_q \tag{22}$$

Substituting Eqn. (22) into Eqn. (19), we obtain

$$\nabla_u f \cdot (\Delta \boldsymbol{u}_r + \Delta\lambda \, \Delta \boldsymbol{u}_q) + \nabla_\lambda f \, \Delta\lambda = -\bar{f} \tag{23}$$

from which we deduce

$$\Delta\lambda = -\frac{\bar{f} + \nabla_u f \cdot \Delta \boldsymbol{u}_r}{\nabla_\lambda f + \nabla_u f \cdot \Delta \boldsymbol{u}_q}. \tag{24}$$

In the case of a load-control procedure, it is finally found

$$\Delta\lambda = -\bar{f} = c - \bar{\lambda} \tag{25}$$

Eqns. (22) and (25) allow for the iterative correction of the initial point $\boldsymbol{u} = \bar{\boldsymbol{u}}$ and $\lambda = \bar{\lambda}$ until convergence is achieved (Fraternali et al., 2015a).

5. Tensegrity modeling of the response to wind loads

The present section employs the path-following procedure described in Sect. 4 to perform a numerical study of the response of a mast element subjected to permanent dead loads and follower wind forces acting in the y–z plane. The analysis assumes that the roof deployment mechanism is locked in a configuration corresponding to a prescribed value of the tilting angle α. It begins with an examination of the load–deflection curves exhibited by the system under increasing wind intensity and subsequently addresses the tensegrity-based modeling of the associated vibration modes for the three configurations shown in Fig. 1(b). As already noted, the investigation of drag-type wind forces acting along the longitudinal x-axis, as well as the analysis of the wind-induced response of the solar membrane accounting for both normal pressure and drag effects, lie beyond the scope of the present study and are addressed to future work

5.1. Load–deflection curves up to failure of the structural mast

Let us study the response of a structural mast for values of the wind-load multiplier λ increasing from zero to 3.5. Consistent with the follower-force assumption for normal wind loading, the wind forces are kept perpendicular to the current configuration of bar 7–17 throughout the path-following process. In both the downward and upward wind-loading conditions, such forces are assumed to result from the combined action of positive and negative wind pressures acting on the two faces of the roof membrane (windward and leeward sides). The force–displacement curves were computed in incremental steps of 0.05 in the wind-load multiplier λ, starting from the configuration under pure permanent forces $\boldsymbol{g}$ and continuing until the attainment of an ultimate limit state in the first member, either in compression (for compressed GLT members) or in tension (for tensile GLT members and suspension cables). This condition is defined as the failure state of the system.

Referring to the downward wind loading condition, Figure 5 shows the load– deflection curves relating λ to the increment of the vertical component of the displacement of tip node 17, measured with respect to the initial configuration with zero wind forces and denoted as Δw_{tip}. Two values of the ratio p between the pretension force applied to suspension cable 6–17 and the design load $N_{t,\text{Rd}}$, were considered, namely $p = 0.05$ and $p = 0.50$. The case with $p = 0.05$ is examined to analyze the response of the mast under low pretensioning of the suspension cables, whereas the case with $p =$

0.50 corresponds to a representative pretensioning level. Using the notation introduced in Sect. 3, we prescribe $x_1 = pN_{t,\mathrm{Rd}}/\bar{\ell}$, where $\bar{\ell}$ denotes the free length of cable 6–17. In the remainder of the paper, we adopt the notation λ_{fail} and λ_{slack} to denote the values of λ corresponding to system failure and to the occurrence of the first slackening event, respectively.

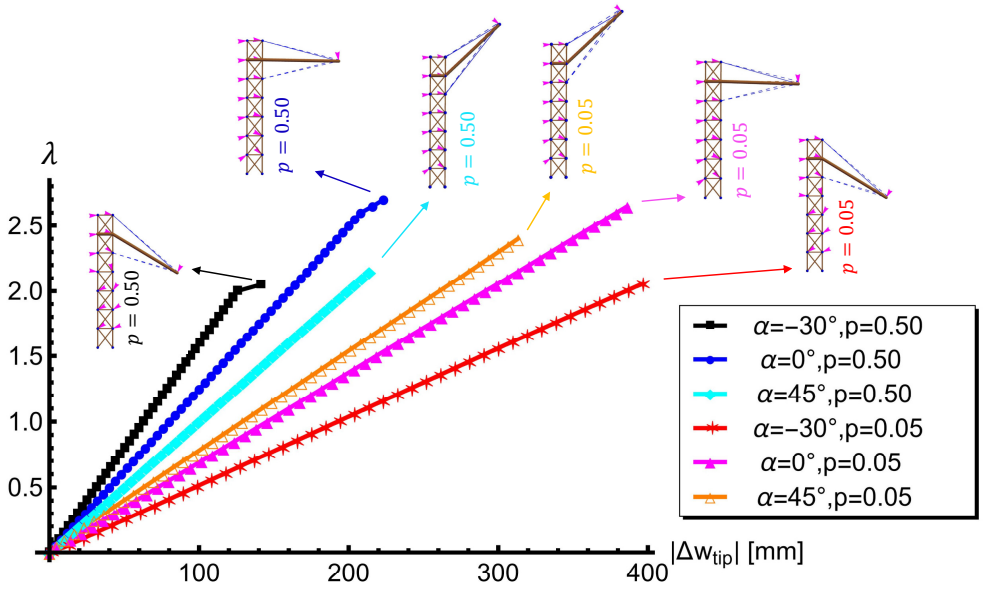

Figure 5: Load–deflection curves up to failure of the structural mast under increasing downward-acting wind forces. The quantity Δw_{tip} represents the incremental vertical displacement of node 17, measured from the reference configuration with zero wind forces. The quantity p denotes the ratio between the pretension force applied to the suspension cable 6-17 and the ULS design tensile load of this elements. The deformed shapes shown in the insets refer to the failure configurations, characterized by the attainment of a tensile ULS in the cable 8–17; arrows indicate displacements with respect to the initial configuration in the absence of wind forces (nodal displacement not amplified). The deformed configurations of the suspension cables at the failure state are indicated by dashed lines when the cables are slack. The undeformed configurations of all members are shown using dashed lines.

The results presented in Fig. 5 show bending points in the load–deflection curves when cable 6–17 becomes slack (i.e., when its tensile axial force reduces to zero). This condition implies that the cable is no longer able to carry additional axial force once slackening occurs under downward wind loading, while cable 8–17 remains active. The responses appear to be linear both

before and after the bending point, when present. Focusing first on the cases with $p = 0.50$, bending points are observed in the load–deflection curves for $\alpha = 0$ and $\alpha = -30°$ at $\lambda_{\text{slack}} = 2.60$ and $\lambda_{\text{slack}} = 2.00$, respectively. In these cases, failure subsequently occurs due to the attainment of a tensile ultimate limit state (TULS) in the suspension cable 8–17 at $\lambda_{\text{fail}} = 2.70$ and $\lambda_{\text{fail}} = 2.05$, respectively. Such a failure condition is observed in all the downward wind loading cases examined in the present section. When $\alpha = 45°$, the suspension cables do not become slack prior to failure, which occurs at $\lambda_{\text{fail}} = 2.15$. Turning to the responses for $p = 0.05$, the corresponding load–deflection curves exhibit bending points due to the slackening of cable 6–17 at very low values of λ, ranging from $\lambda_{\text{slack}} \approx 0$ for $\alpha = -30°$ to $\lambda_{\text{slack}} = 0.10$ for $\alpha = 45°$. The early slackening of one of the suspension cables results in a marked reduction in the overall stiffness of the system, which is clearly evident when comparing the load–deflection curves in Fig. 5 corresponding to $p = 0.05$ and $p = 0.50$. For $p = 0.05$, as in the case with $p = 0.50$, failure occurs due to the attainment of a tensile ultimate limit state (TULS) in cable 8–17, with $\lambda_{\text{fail}} = 2.65$, $\lambda_{\text{fail}} = 2.05$, and $\lambda_{\text{fail}} = 2.40$ for $\alpha = 0$, $\alpha = -30°$, and $\alpha = 45°$, respectively.

The maximum incremental vertical displacements of the tip node at failure induced by high wind forces are directed downward and range from approximately 141 mm for $\alpha = -30°$ and $p = 0.50$ ($\lambda_{\text{fail}} = 2.05$) to approximately 395 mm for $\alpha = -30°$ and $p = 0.05$ ($\lambda_{\text{fail}} = 2.05$). For the design wind load corresponding to $\lambda = 1$ and for the representative prestress value $p = 0.50$, the absolute value of the tip displacement $|\Delta w_{\text{tip}}|$ is instead equal to 80 mm, 63 mm, and 99 mm for $\alpha = 0$, $\alpha = -30°$, and $\alpha = 45°$, respectively. These values imply that the ratio between the tip displacement and the length of the main beam 7–17 does not exceed 1/200 under ULS wind loads. It should be emphasized that these deflections have been computed under wind loads corresponding to the ultimate limit state ($\gamma_Q = 1.5$), whereas the Italian structural code NTC (2018) requires verification of structural deformability at the serviceability limit state, with the wind-load partial factor γ_Q not exceeding unity. By adopting a linear rescaling of the deflections induced by wind forces to a value of γ_Q equal to one, which can be safely applied to the results shown in Fig. 5, the resulting ratio between the tip displacement and the length of the main beam 7–17 does not exceed 1/300 for the analyzed cases with $p = 0.50$ and $\lambda = 1$. It is also worth noting that the vertical displacements of tip node 17 under permanent loads only (i.e., in the absence of wind forces) range from approximately 17 mm to 23 mm

for the examined values of α and p.

The load–deflection curves for the upward wind-loading condition are shown in Fig. 6. It is worth highlighting that, under this loading condition, failure always occurs due to the attainment of a tensile ultimate limit state in cable 6–17 for all the examined cases. Under increasing upward wind forces, slackening may occur in cable 8–17, whereas cable 6–17 progressively increases its tensile force with respect to the pretensioned state, up to failure. For upward wind loading and $p = 0.50$, the values of λ_{fail} are equal to 3.10, 2.55, and 1.95 for $\alpha = 0$, $\alpha = -30°$, and $\alpha = 45°$, respectively. For $p = 0.50$, $\alpha = 0$, and $\alpha = -30°$ the suspension cables do not become slack prior to failure, while for $\alpha = 45°$ with $p = 0.50$ the slackening of cable 8-17 is observed at $\lambda_{\text{slack}} = 1.40$. With regard to the cases with the low pretensioning ratio $p = 0.05$, the following values were observed: $\lambda_{\text{fail}} = 3.15$ and $\lambda_{\text{slack}} = 0.55$ for $\alpha = 0$; $\lambda_{\text{fail}} = 3.15$ and $\lambda_{\text{slack}} = 0.65$ for $\alpha = -30°$; and $\lambda_{\text{fail}} = 1.90$ and $\lambda_{\text{slack}} = 0.30$ for $\alpha = 45°$. In the present case, the values of Δw_{tip} refer to upward-directed vertical displacements.

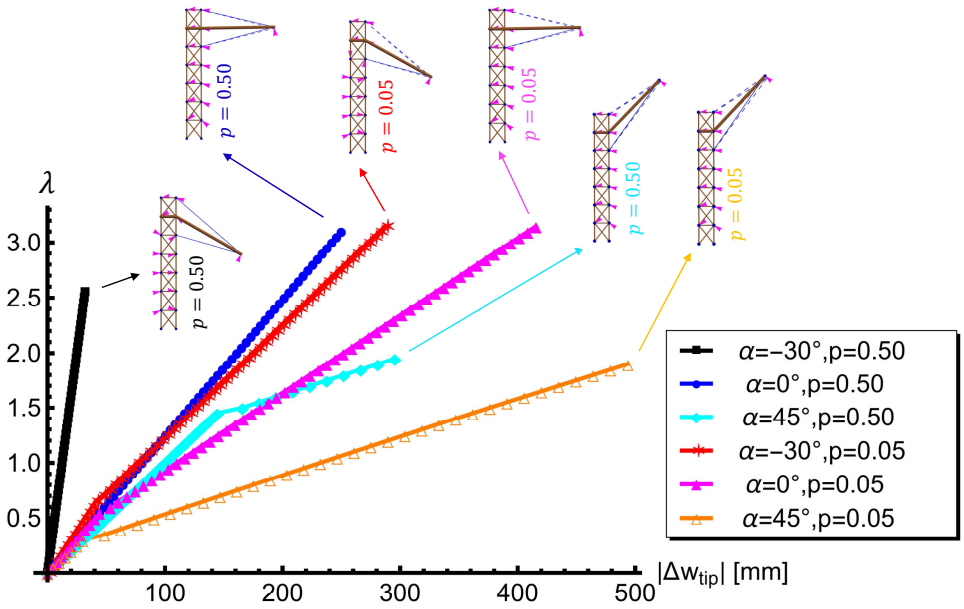

Figure 6: Load–deflection curves up to failure of the structural mast under increasing upward-acting wind forces.

The displacements at failure under high wind loads range from approx-

imately 32 mm for $\alpha = -30°$ and $p = 0.50$ to approximately 494 mm for $\alpha = 45°$ and $p = 0.05$. For $\lambda = 1$ and $p = 0.50$, the absolute value of the tip displacement $|\Delta w_{\text{tip}}|$ is equal to 80 mm, 12 mm, and 100 mm for $\alpha = 0$, $\alpha = -30°$, and $\alpha = 45°$, respectively. Also in the upwind loading case, as under downwind forces, the results presented in Fig. 6 highlight a marked reduction in the overall stiffness of the system when the prestress factor p is reduced from 0.50 to 0.05, due to the early slackening of one of the suspension cables.

5.2. Modal vibration analysis

We now present an analysis of the undamped vibration modes and the associated natural frequencies f corresponding to the configuration under permanent loads, based on the tensegrity model of a structural mast. A three-dimensional finite element (FEM) study of the corresponding vibration modes of a modular three-dimensional stadium element is presented in the subsequent Sect. 6.

Figure 7 shows the results obtained for the first three vibration modes of the tensegrity model with $\alpha = 0$ and $p = 0.50$. One observes that the natural frequencies associated with these modes are well separated from each other, which is a desirable feature in view of structural health monitoring applications (Ashwear et al., 2016). In particular, the frequency of the first mode is $f_1 = 2.133$ Hz, while those of the second and third modes are $f_2 = 4.181$ Hz and $f_3 = 14.311$ Hz, respectively.

The frequencies associated with the next three higher modes (not shown in Fig. 7) are $f_4 = 23.030$ Hz, $f_5 = 32.251$ Hz, and $f_6 = 42.434$ Hz. The shape of the first vibration mode closely resembles the deformed configurations observed under wind loading in the previous section. When the prestress level is reduced to $p = 0.05$, the resulting natural frequencies differ from those obtained for $p = 0.50$ by less than 0.003%, indicating a negligible influence of the prestress level on the natural frequencies of the structure under consideration.

For the cases with $\alpha = -30°$ and $\alpha = 45°$, respectively, and still assuming $p = 0.50$, vibration mode shapes similar to those obtained for $\alpha = 0$ were observed. These modes are shown in Figures 8-9.

The corresponding natural frequencies are as follows: $f_1 = 2.261$ Hz, $f_2 = 3.672$ Hz, and $f_3 = 14.084$ Hz for $\alpha = -30°$ and $p = 0.50$; $f_1 = 1.925$ Hz, $f_2 = 3.840$ Hz, and $f_3 = 14.139$ Hz for $\alpha = 45°$ and $p = 0.50$. The fact that the first fundamental frequency is appreciably greater than 1 Hz suggests that the

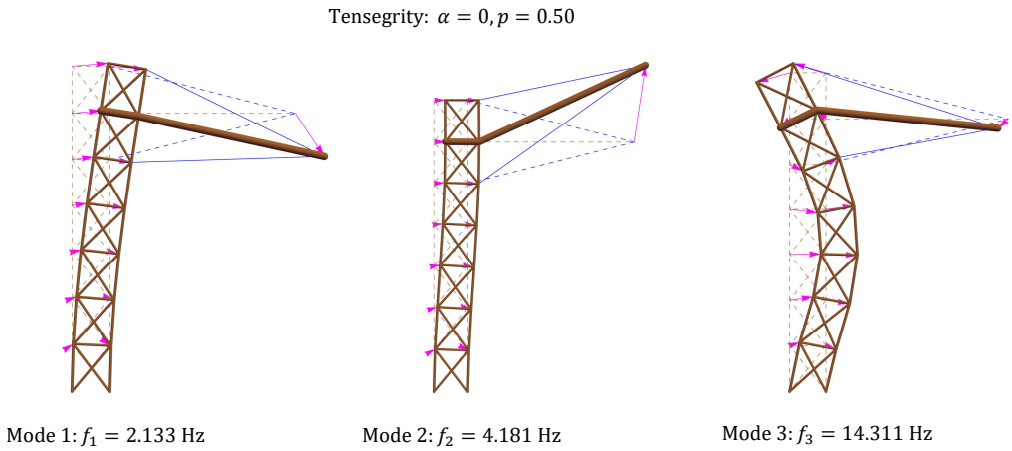

Figure 7: First three vibration modes and corresponding natural frequencies of the structural mast for $\alpha = 0$ and $p = 0.50$, as computed through tensegrity-based modeling.

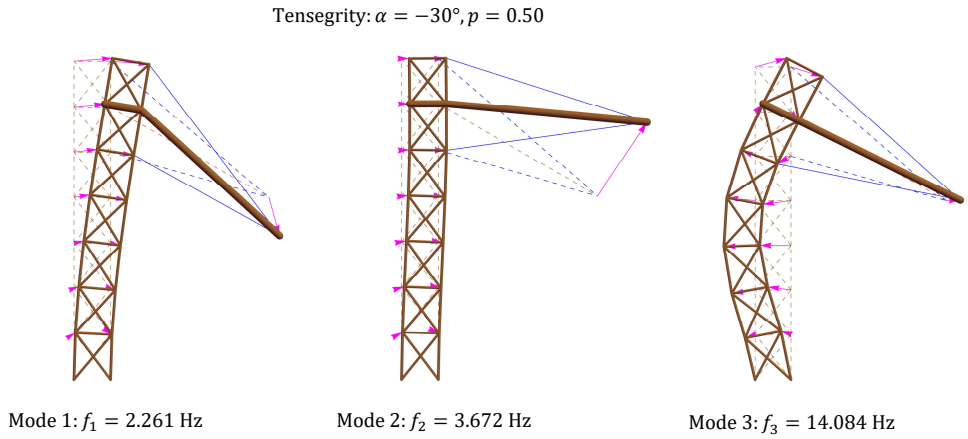

Figure 8: First three vibration modes and corresponding natural frequencies of the structural mast for $\alpha = -30°$ and $p = 0.50$, as computed through tensegrity-based modeling.

mast structure is not particularly susceptible to resonance-type phenomena under wind loading (Holmes and Bekele, 2021). Consequently, wind effects may be reasonably treated as quasi-static in a preliminary assessment of this structural element.

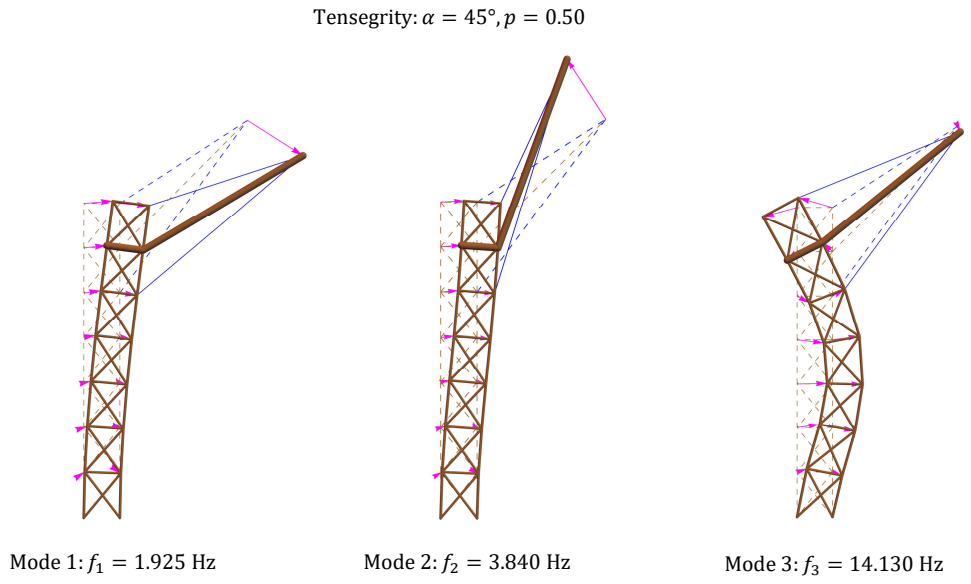

Figure 9: First three vibration modes and corresponding natural frequencies of the structural mast for $\alpha = 45°$ and $p = 0.50$, as computed through tensegrity-based modeling.

6. Finite element modeling of a stadium module

A three-dimensional finite element analysis of the undamped vibration modes of the modular stadium structure shown in Fig. 2 was performed using the commercial software SAP2000® (Computers and Structures, Inc., 2016) for $\alpha = 0$, with the deployment mechanism assumed to be locked. All members were modeled as beam (frame) elements connected to each other and to the ground through hinged joints, in order to capture vibration modes involving bending-type responses of the structural elements. The presence of stadium modules adjacent to the one under investigation was taken into account by constraining the terminal nodes in the x direction. The GLT material was modeled as orthotropic elastic, and the mechanical properties reported in Sect. 2 were adopted for the timber members, while the properties specified for the steel wire ropes were used for the suspension cables. The longitudinal GLT links were assigned a cross section of 200 mm × 200 mm as a first approximation. The analysis was performed using the linear modal analysis function of SAP2000® for $p = 0.50$, starting from the deformed configuration obtained at the end of a static analysis of the load

case corresponding to the application of permanent loads with $\gamma_G = 1.30$.

Fig. 10 shows the first three vibration modes obtained from the finite element analysis, which correspond to the natural frequencies $f_1 = 2.246$ Hz, $f_2 = 3.301$ Hz, and $f_3 = 3.625$ Hz. It is observed that the first vibration mode predicted by the FEM closely resembles that obtained from the tensegrity-based modeling, with a slightly higher natural frequency (2.246 Hz versus 2.133 Hz; compare Fig. 10 with Fig. 7). The higher fundamental frequency predicted by the FEM can be attributed to the stiffening effect of the longitudinal bracing elements running in the two parallel vertical planes containing the mast columns, which respond alternately in tension and compression during structural oscillations and are not included in the tensegrity model of a single mast element.

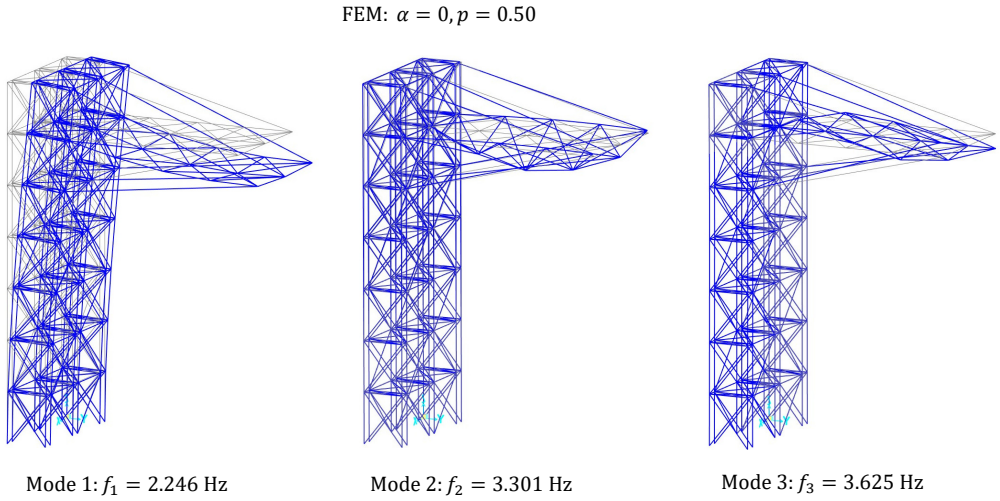

Figure 10: First three vibration modes and corresponding natural frequencies of a modular component of the stadium structure for $\alpha = 0$ and $p = 0.50$, computed using a finite element model.

The second vibration mode predicted by the FEM is associated with flexural vibrations of the horizontal GLT bracing members that longitudinally connect the main beams, while the third mode is associated with torsional vibrations of these braces. Such modes cannot be captured by the tensegrity model, since it refers to a single mast element. The second natural frequency predicted by the FEM is well separated from the fundamental frequency, while the second and third modes exhibit closer spacing but remain suffi-

ciently separated from one another. As noted earlier, a noticeable separation of the modal frequencies is beneficial for structural health monitoring applications (Ashwear et al., 2016). Finally, the good agreement between the fundamental mode shape predicted by the FEM and that obtained from the tensegrity model of a mast element indicates that the latter can be safely employed to study the structural response under normal wind loading, within a preliminary quasi-static approach.

7. Concluding remarks

A detailed study is presented on the mechanical response of key modular components of an innovative solar stadium structure made of glued laminated timber and equipped with a tiltable roof membrane of remarkable span. The results of a numerical investigation of the structural response of a tensegrity-based model of a representative mast element forming the stadium structure show that the system remains stable under high wind loads, especially when the prestress is properly designed. In the most unfavorable configuration, collapse of the suspension cables occurs for a wind-load multiplier close to 2 with respect to a reference set of wind forces. The maximum observed vertical displacements of the roof tip are safely sustainable by the adopted solar panels (Solbian Manual, 2025). The tensegrity-based modeling framework further indicates that the natural vibration modes of the mast structure exhibit sufficiently separated modal frequencies, with the fundamental frequency being on the order of 2 Hz. These results were compared with those obtained from a three-dimensional finite element analysis of a modular element of the stadium structure, showing good agreement with respect to the first (fundamental) vibration mode.

The present study admits several relevant extensions and generalizations, both from a structural perspective and with regard to the energetic and sustainability aspects of the proposed stadium system. A comprehensive mechanical investigation of innovative tensile membranes equipped with photovoltaic devices and subjected to both normal and drag wind forces is deferred to future work. Such studies are expected to involve both advanced numerical modeling and experimental investigations in wind tunnels (Glück et al., 2003; Bridgens and Birchall, 2012; Scotta et al., 2016; Brusco et al., 2024). Additional structural aspects deserving further investigation include a three-dimensional generalization of the tensegrity model examined in the present work, a detailed analysis of the connections between timber members (Dong

et al., 2020b), and the assessment of loading conditions not addressed in this study, such as drag-type wind forces, concentrated loads, snow loads, and seismic actions (Milošević et al., 2024; Charandabi et al., 2025a). Future work on the energetic performance of the system will focus on estimating the solar energy harvesting capacity of the photovoltaic membrane, accounting for variable tilting angles throughout the year and different hours of the day (Charandabi et al., 2025a). Finally, a comprehensive Life Cycle Assessment (LCA) of the proposed solar timber stadium also requires further investigation, including the evaluation of carbon emissions associated with construction, operation, and post-event activities, as well as the contribution of the solar roof to on-site energy generation (Xuan et al., 2025; Dong et al., 2020b; Dodoo et al., 2014; Daddi et al., 2025).

Acknowledgments

The authors gratefully acknowledge Dr. Massimo Bernardotto and the technical staff of Sirtef srl for their valuable assistance in the selection and mechanical characterization of the steel wire ropes analyzed in the present study. They also wish to sincerely thank Dr. Gerry Danza of IXRAY Ltd. for his valuable collaboration on the preliminary design of the tensile membrane employed in this work.

Data availability

Information on the CAD models and the Mathematica® codes used in this study is available from the corresponding author upon request.

Funding

This work was supported by the National Recovery and Resilience Plan (NRRP), Mission 4, Component 2, Investment 1.1, Call for tender No. 104 published on 2.2.2022 by the Italian Ministry of University and Research (MUR), funded by the European Union – NextGenerationEU – Project Title 'Innovative tensegrity lattices and architectured metamaterials' (ILAM) – 20224LBXMZ – CUP D53D23003020006 (FF); - Grants Assignment Decree No. 961 adopted on 30/06/2023 by the Italian Ministry of Ministry of University and Research (MUR). It has also been supported by the National Recovery and Resilience Plan (NRRP), Mission 4, Component 2, Investment

1.1, Call for tender No 1409 published on 14.9.2022 by the Italian Ministry of University and Research (MUR), funded by the European Union – NextGenerationEU – Project Titles 'Sustainable composite structures for energy harvesting and carbon-storing buildings' (SUSTBUILD) – P2022PE8BT – CUP D53D23018440001 (GC); 'Stabilization of contaminated soils' (STABSOIL) – P2022CR8AJ – CUP D53D23018180001 (FF) – Grants Assignment Decree No. 1385 adopted on 01/09/2023 by the Italian Ministry of Ministry of University and Research (MUR). FF also acknowledges support by the Italian Ministry of Foreign Affairs and International Cooperation within the Italy-USA Science and Technology Cooperation Program 2023–2025, Project 'Next-generation green structures for natural disaster-proof buildings', grant number US23GR15. RNC thanks the Italian National Group for the Mathematical Physics (GNFM) of the National Institute for Advanced Mathematics (INdAM) and the Italian Dottorato di Interesse Nazionale 'Photovoltaics'.

Author Contributions

Rana Nazifi Charandabi: Conceptualization, resources, data curation, software, formal analysis, supervision, validation, investigation, visualization, methodology, project administration, writing–original draft, writing–review and editing. Gerardo Carpentieri: Data curation, software, validation, investigation, visualization, methodology, writing–original draft, writing–review and editing. Fernando Fraternali: Conceptualization, resources, data curation, software, formal analysis, supervision, validation, investigation, visualization, methodology, project administration, writing–original draft, writing–review and editing, funding acquisition. All authors approved the final version of the manuscript and agree to be accountable for all aspects of the work.

References

Alaoui, M., Zarraa, F.A.T.A., 2025. Sustainable strategies for optimizing the reduction of ghg emissions in qatar's football stadiums. Greenhouse Gases: Science and Technology , e2363.

Ashwear, N., Tamadapu, G., Eriksson, A., 2016. Optimization of modular tensegrity structures for high stiffness and frequency separation requirements. International Journal of Solids and Structures 80, 297–309. doi:10.1016/j.ijsolstr.2015.11.017.

BEAR Stadiums, . Bear stadiums – modular and sustainable stadium solutions. https://www.bearstadiums.com/en. Accessed January 12 2026.

Belytschko, T., Liu, W.K., Moran, B., Elkhodary, K., 2014. Nonlinear finite elements for continua and structures. John wiley & sons.

Binderholz GmbH, 2024. Glulam (glt) catalogue. https://www.binderholz.com/fileadmin/user_upload/books/en/glulam/4/index.html. Online catalogue, accessed January 12 2026.

Bridgens, B., Birchall, M., 2012. Form and function: The significance of material properties in the design of tensile fabric structures. Engineering structures 44, 1–12.

Brusco, S., Bin, H.Y., Lo, Y.L., Piccardo, G., 2024. Transient aerodynamics of a square cylinder under downburst-like accelerating flows reproduced in a multiple-fan wind tunnel. Journal of Fluids and Structures 124, 104038.

Charandabi, R.N., Babilio, E., Carpentieri, G., Spagnuolo, G., Amendola, A., Fraternali, F., 2025a. A tensegrity structure for a solar stadium roof with sun-tracking capability. Thin-Walled Structures , 113033.

Charandabi, R.N., de Castro Motta, J., Carpentieri, G., Babilio, E., Bo, J.B., Fantuzzi, N., Fraternali, F., 2025b. Deployability, mechanical response, and energy harvesting capacity of a novel solar roof for sports stadiums. Developments in the Built Environment , 100771.

Computers and Structures, Inc., 2016. SAP2000: Integrated Finite Element Analysis and Design of Structures. Computers and Structures. URL: https://docs.csiamerica.com/manuals/sap2000/CSiRefer.pdf.

Daddi, T., Marrucci, L., Todaro, N.M., Iraldo, F., 2025. How polluting is professional football? the environmental footprint of a football match calculated with a life cycle assessment. Sport, Business and Management: An International Journal , 1–23.

Dodoo, A., Gustavsson, L., Sathre, R., 2014. Lifecycle carbon implications of conventional and low-energy multi-storey timber building systems. Energy and buildings 82, 194–210.

Dong, W., Li, M., Lee, C.L., MacRae, G., Abu, A., 2020a. Experimental testing of full-scale glulam frames with buckling restrained braces. Engineering Structures 222, 111081.

Dong, Y., Qin, T., Zhou, S., Huang, L., Bo, R., Guo, H., Yin, X., 2020b. Comparative whole building life cycle assessment of energy saving and carbon reduction performance of reinforced concrete and timber stadiums—a case study in China. Sustainability 12, 1566.

European Committee for Standardization - EC5, 2004. Eurocode 5: Design of timber structures – part 1-1: General – common rules and rules for buildings. EN 1995-1-1:2004+A2:2014.

European Committee for Standardization (CEN) - EN 12385, . EN 12385: Steel wire ropes – Safety. Parts 1–10.

FIFA, 2023. Stadium guidelines. https://inside.fifa.com/innovation/stadium-guidelines/general-process-guidelines/design/sustainability-design. Accessed: January 12 2026.

Fraternali, F., Carpentieri, G., Amendola, A., 2015a. On the mechanical modeling of the extreme softening/stiffening response of axially loaded tensegrity prisms. Journal of the Mechanics and Physics of Solids 74, 136–157.

Fraternali, F., De Chiara, E., Skelton, R., 2015b. On the use of tensegrity structures for kinetic solar facades of smart buildings. Smart materials and structures 24, 105032.

Glück, M., Breuer, M., Durst, F., Halfmann, A., Rank, E., 2003. Computation of wind-induced vibrations of flexible shells and membranous structures. Journal of Fluids and Structures 17, 739–765.

Holmes, J.D., Bekele, S.A., 2021. Wind Loading of Structures: Fourth Edition. CRC Press.

IXRAY Ltd., 2024. Ixray ltd. official website. https://www.ixray-ltd.com. Accessed: January 12, 2026.

Marchwiński, J., Milošević, V., Stefańska, A., Lucchi, E., 2023. Irradiation analysis of tensile membrane structures for building-integrated photovoltaics. Energies 16, 5945.

Milošević, V., Marchwiński, J., Kopyłow, O., 2024. Dependance of membrane stress on the supports geometry of the barrel-vault shaped tensile membrane structures. Builder 28, 46–49.

Nagase, K., Skelton, R., 2014. Minimal mass tensegrity structures. Journal of The International Association for Shell and Spatial Structures 55, 37–48. doi:10.1117/12.2044869.

NTC, 2018. D.M. 17/01/2018. Norme Tecniche per le Costruzioni (in Italian). Gazzetta Ufficiale, n. 42 del 20/02/2018, Supplemento ordinario n.8 42.

Scotta, R., Lazzari, M., Stecca, E., Di Massimo, R., Vitaliani, R., 2016. Membranes with embedded photovoltaic flexible cells: Structural and electrical performances under uniaxial and biaxial stresses. Composite Structures 157, 111–120.

Serge Ferrari Group, 2024. Flexlight xtrem tx30-ii tensile membrane. https://www.sergeferrari.com/vi/productsflexlight-range/flexlight-xtrem-tx30-ii. Accessed: January 12, 2026.

Sirtef srl, 2026. Steel Wire Ropes. https://www.sirtef.it/en/products/steel-wire-ropes/. [Accessed: January 12 20266].

Solbian, 2025. SunBender solar panels. https://blog.solbian.eu/en/sunbender. [Accessed: January 12 2026].

Solbian Manual, 2025. Solbian Solar Panel User's Manual . https://www.emarineinc.com/Shared/pdf/Solbian/Solbian-Users-Manual.pdf. [Accessed: January 12 2026].

Sport & Impianti, 2023. Sustainability in the new fifa guidelines. https://www.sporteimpianti.it/en/main/tsport-en/tsport-index/reportage-en/sustainability-in-the-new-fifa-guidelines/. Accessed: January 12 2026.

Sustainability Magazine, 2023. What are the world's most sustainable sports stadiums? https://sustainabilitymag.com/news/what-are-the-worlds-most-sustainable-sports-stadiums. Accessed: January 12 2026.

Tahmasebinia, F., Chen, E., Huang, A., Li, J., 2023. Designing lightweight stadium roofing structures based on advanced analysis methods. Sustainability 15, 3612.

Timoshenko, S.P., Gere, J.M., 2012. Theory of elastic stability. Courier Corporation.

Xuan, S., Qin, Y.N., Zhou, J.X., Wu, J.P., 2025. The impact of stadiums on carbon emissions: A systematic review. Polish Journal of Environmental Studies .